Chemical Engineering Science 302 (2025) 120785

Contents lists available at ScienceDirect

Chemical Engineering Science

journal homepage: www.elsevier.com/locate/ces

Activation and Zr precursor influence on UiO-66-NH_2 composites for efficient cationic and anionic dye removal

Sherif Hegazy [a], Ayoub Ghannami [b], Glaydson S. dos Reis [c,d], Tao Hu [a], Rachid Brahmi [b], Sari Tuomikoski [a], Ulla Lassi [a], Varsha Srivastava [a,*]

[a] Research Unit of Sustainable Chemistry, University of Oulu, P.O. Box 4300, FI-90014 Oulu, Finland
[b] Laboratory of Coordination and Analytical Chemistry (LCCA), University Chouaïb Doukkali, Avenue des Facultés, 24000 El Jadida, Morocco
[c] Laboratory of Industrial Chemistry and Reaction Engineering, Faculty of Science and Engineering, Åbo Akademi University, 20500 Åbo/Turku, Finland
[d] Biomass Technology Centre, Department of Forest Biomaterials and Technology, Swedish University of Agricultural Sciences, SE-90183 Umeå

ARTICLE INFO

Keywords:
Activation
Anionic dye
Cationic dye
UiO-66-NH_2
Textural properties
Water treatment

ABSTRACT

This study investigates the synthesis of UiO-66-NH_2@HTC composites, focusing on the control of surface charge, textural properties, and crystallinity. Surface charge modification was achieved through activation processes to enhance affinity for specific pollutants. By utilizing $ZrCl_4$ and $ZrOCl_2{\cdot}8H_2O$ precursors, the textural properties were optimized, leading to higher mesopore content and improved crystallinity with the $ZrOCl_2{\cdot}8H_2O$ precursor. The UiO-66-NH_2($ZrCl_4$)@HTC composite exhibited a crystallinity of 51.7 %, with 40 % mesopores and 57 % micropores, while the UiO-66-NH_2($ZrOCl_2$)@HTC composite showed a crystallinity of 60 %, consisting of 60 % mesopores and 37 % micropores. Adsorption followed the Langmuir isotherm model, with maximum adsorption capacities of 263.1 mg/g for methylene blue (MB) and 277.77 mg/g for Congo red (CR), driven by hydrogen bonding and electrostatic interactions. The activated UiO-66-NH_2@HTC composites demonstrated remarkable reusability. These findings emphasize the significant role of surface charge modification, pore structure optimization, and crystallinity enhancement in developing high-performance adsorbents.

1. Introduction

Metal–organic frameworks (MOFs) are a class of porous materials characterized by metal clusters acting as nodes and organic ligands serving as linkers between these nodes (Absalan et al., 2024). MOFs are renowned for their exceptional structural tunability, prominent porosity, large surface areas, and tailorable properties (Ben Moussa, 2024; Yu et al., 2021). These features confer several advantages over other porous materials, such as zeolites, activated carbon, and porous metals, including ease of processing, availability of exposed catalytic sites, stability of the frameworks, and relatively straightforward synthesis procedures (Peng et al., 2023). As a result, MOFs are highly sought after for a wide range of applications, including gas separation (Chen et al., 2023), water remediation (Ahmadijokani et al., 2022; Lei et al., 2024), catalytic processes (Chaouiki et al., 2024), energy storage (Shahzad et al., 2023), and drug delivery (Rabiee, 2023).

Among zirconium-based MOFs, UiO-66 is particularly notable for its high stability and versatile framework, consisting of cationic $Zr_6O_4(OH)_4$ nodes linked to terephthalic acid through 12-coordinated bonds (Gómez-Avilés et al., 2023). However, while the UiO-66 framework is robust, its adsorptive efficiency and physicochemical properties are significantly influenced by the choice of Zr precursors and the activation methods employed (Kebede Gurmessa et al., 2023; Timofeev et al., 2023). Previous studies have primarily focused on the synthesis of UiO-66 using zirconium chloride or zirconium oxoclusters, with limited investigation into how different precursors can be optimized to enhance both microporosity and mesoporosity simultaneously (Kubo et al., 2024; Cox et al., 2023). Moreover, while activation processes have been applied to improve the surface properties of MOFs, there is a lack of comprehensive studies exploring the combined effects of acidic and basic activations on UiO-66-NH_2 composites. Additionally, the incorporation of carbon derived from hydrothermal carbon (HTC) into the UiO-66-NH_2 framework remains underexplored, particularly regarding its potential to enhance adsorption capacities for both cationic and anionic dyes.

Various strategies have been explored in previous studies to improve the physicochemical structure of UiO-66. For instance, Zhou et al. (Zhou et al., 2023) employed two distinct methods – Ar and H_2 plasma

* Corresponding author.
E-mail address: varsha.srivastava@oulu.fi (V. Srivastava).

https://doi.org/10.1016/j.ces.2024.120785
Received 25 June 2024; Received in revised form 15 September 2024; Accepted 29 September 2024
Available online 30 September 2024

treatments – to induce defects in UiO-66, enhancing its adsorptive properties. Rafael et al. (Solís et al., 2022) used a fast microwave-assisted method to compare the effects of two Zr precursors, Zr oxychloride and organic Zr alkoxide, observing that Zr oxychloride led to larger particle and crystal sizes. Marco et al. (Taddei et al., 2020) focused on the effects of a single precursor on UiO-66 synthesis, while Luu et al. (Luu et al., 2015) studied the synthesis of UiO-66-NH_2 with functional group incorporation to enhance CH_4 adsorption, finding that the incorporation of these functional groups led to a decrease in the surface area but an increase in adsorptive properties. Wu et al. (Wu et al., 2024) explored the relationship between the structural characteristics of Zr-based porphyrinic MOFs and their adsorption behaviour, emphasizing the importance of pore structure and size. Additionally, Huang et al. (Huang et al., 2024) designed a cationic MOF specifically for the selective removal of anionic pollutants.

This study addresses existing gaps by investigating the synthesis of UiO-66-NH_2 using two different zirconium precursors: zirconium tetrachloride ($ZrCl_4$) and zirconium oxychloride octahydrate ($ZrOCl_2{\cdot}8H_2O$). This approach offers a novel perspective on controlling specific surface area, pore structure, surface functional groups, textural properties, and crystallinity in UiO-66-NH_2 composites. Furthermore, by employing both acidic and basic activation methods, this research aims to enhance the adsorptive efficiency of the composites for the removal of Congo red (CR) and methylene blue (MB) dyes from aqueous solutions. The incorporation of HTC into the synthesis of UiO-66-NH_2@HTC composites provides an additional structural enhancement, potentially leading to superior adsorption performance. HTC, a process that converts biomass into carbon-rich materials under moderate temperatures and pressures, further improves the adsorptive properties of the MOFs (Cavali et al., 2023).

2. Experimental section

2.1. Materials

Spruce bark sawdust was sourced from a sawmill in northern Sweden. All chemicals used in this study were of analytical grade and were utilized without further purification. Hydrochloric acid (HCl) and sodium hydroxide (NaOH) were procured from Merck (Germany). Zirconium (IV) chloride anhydrous ($ZrCl_4$, 99.99 % purity) and zirconyl chloride octahydrate ($ZrOCl_2{\cdot}8H_2O$, 98 % purity) were obtained from Sigma Aldrich (Germany). 2-Aminoterephthalic acid ($C_8H_7NO_4$, >98 % purity) was supplied by TCI (Japan). CR and MB dyes were acquired from Fisher Scientific (UK). N,N-Dimethylformamide (DMF, >98 % purity), acetonitrile (ACN, maximum 0.001 % water), and ethanol absolute were obtained from VWR (UK).

2.2. Synthesis of UiO-66-NH_2@HTC

HTC was prepared by mixing 20 g of spruce bark with 200 mL of deionized (DI) water. The mixture was placed into a hydrothermal carbonization vessel and heated at 250 °C for 3 h, corresponding to a pressure of 47 bar. Then, 271.72 mg (1.50 mmol) of 2-aminoterephthalic acid and 600 mg of HTC were mixed in 20 mL of DMF and stirred for 20 min in a 250-mL screw-cap bottle. A separately prepared solution of 251.6 mg (1.08 mmol) of $ZrCl_4$ in 10 mL of DMF was then added to the previous mixture. The bottle was capped, and the mixture was stirred at 80 °C for 12 h. Afterwards, the mixture was filtered, washed with ACN, and subjected to a solvent exchange under autogenous pressure for 2 h using heated ACN at 80 °C. The product was then filtered and dried in an oven at 80 °C for 2 h. The final product, UiO-66-NH_2@HTC, was obtained in a yield of 820 mg (73 %), corresponding to an approximate HTC to UiO-66-NH_2 ratio of 2.73:1. The same procedure was repeated using $ZrOCl_2{\cdot}8H_2O$ instead of $ZrCl_4$ as the precursor.

2.3. Chemical activation of UiO-66-NH_2@HTC

The MOFs were activated by adding either 2 mL of 37 % HCl or 2 mL of 0.1 M NaOH to the mixture, as presented in Table 1.

2.4. Characterization

The characterization of all samples was carried out using advanced analytical techniques at the Centre for Material Analysis, Research Unit of Sustainable Chemistry and Research Unit of Environmental and Chemical Engineering, University of Oulu, Finland. Detailed specifications for each instrument are summarized in Table 2.

2.5. Adsorption studies

In the adsorption experiments, the concentrations of both MB and CR dyes were quantified spectrophotometrically at their wavelengths of maximum absorbance: λ_{max} = 663 nm for MB. For CR, the wavelength varied with pH, showing λ_{max} = 568 nm at pH≥7 and λ_{max} = 499 nm at pH≤5. In each experiment, 0.02 g of each adsorbent sample was added to 20 mL of 30 mg/L dye solutions at varying pH values (3, 5, 7, and 9). Additionally, various parameters including the effect of contact time (1, 2, 3, 4, 5, 6, 12, and 24 h), initial dye concentrations (25 mg/L, 50 mg/L, 100 mg/L, 150 mg/L, 250 mg/L, 400 mg/L, 550 mg/L, and 700 mg/L), and temperature (22 °C, 35 °C, 45 °C, and 55 °C) were examined. Adsorption kinetics, isotherms, and thermodynamics were investigated through batch adsorption experiments. The efficiency of dye removal (% E) and the adsorption capacity (q_e, mg/g) were calculated as follows (Gebre Meskel et al., 2024):

$$\%E = \frac{C_o - C_e}{C_o} \times 100 \quad (1)$$

$$q_e = (C_o - C_e)\frac{V}{m} \quad (2)$$

where C_o and C_e (mg/L) are the initial and final concentrations of dyes, respectively, V(L) represents the volume of the dye solution, and m (g) is adsorbent mass in grams.

2.6. Desorption and reutilization tests

To assess the reusability of the synthesized adsorbents, a series of desorption and regeneration experiments were conducted. Following the adsorption of MB and CR dyes from their aqueous solutions, all samples were subjected to a cleaning process using 0.1 M HCl followed by 70 % ethanol, and then rinsed with deionized water. The cleaned adsorbents were subsequently reused for the removal of both dyes from the aqueous solutions. After each run, the concentration of the dye in the filtrate was determined using UV–visible spectroscopy. The recyclability of the adsorbents was assessed over five cycles for both MB and CR adsorption.

Table 1
Overview of samples, precursors, and activation methods.

Sample code	Precursor	Activation method
HTC	–	–
UiO-66-NH_2($ZrCl_4$)$^+$@HTC	$ZrCl_4$	HCl
UiO-66-NH_2($ZrOCl_2$)$^+$@HTC	$ZrOCl_2{\cdot}8H_2O$	HCl
UiO-66-NH_2($ZrCl_4$)$^-$@HTC	$ZrCl_4$	NaOH
UiO-66-NH_2($ZrOCl_2$)$^-$@HTC	$ZrOCl_2{\cdot}8H_2O$	NaOH

Table 2
List of used analysis technique, equipment and key conditions.

Analysis Technique	Equipment	Key Conditions
DRIFT Spectroscopy	Bruker PMA 50 Vertex 80 V spectrometer (Bruker, Billerica, MA, USA)	Range: 400–4000 cm^{-1}, Resolution: 4 cm^{-1}, Scan Rate: 500 scans/min
X-ray Diffraction (XRD)	PANalytical X'Pert Pro X-ray diffractometer (Almelo, Netherlands)	Cu Kα1 radiation (λ = 1.5406 Å), 45 kV, 40 mA, Step size: 0.017°, 2θ range: 6°–60°
X-ray Photoelectron Spectroscopy (XPS)	Thermo Fisher Scientific ESCALAB 250Xi XPS System (Thermo Fisher Scientific, Waltham, MA, USA)	High-resolution Scan: Pass energy 20 eV, Survey Scan: Pass energy 150 eV, AlKα radiation (1486.7 eV), Spot size: 900 μm
BET Surface Area & Pore Analysis	Micromeritics 3 Flex physisorption instrument (Micromeritics Instruments, Norcross, GA, USA)	Adsorptive: N_2, Analysis Temp.: 77.3 K, Sample Mass: 0.1617 g, Free Space: 57.4323 cm^3, Equilibration Interval: 5 s
Zeiss Sigma field-emission scanning electron microscope (FESEM)	Zeiss Sigma FESEM (Carl Zeiss Microscopy GmbH, Jena, Germany)	5 kV, Magnifications: 150 × to 100,000×
Energy-filtered transmission electron microscope (EFTEM/STEM)	JEOL JEM-2200FS (JEOL Ltd., Akishima, Japan)	200 kV, Sample Prep: Ultrasonic dispersion in ethanol, deposited on carbon-coated copper grid
UV–Visible Spectroscopy	SHIMADZU UV-1800 (Shimadzu Corporation, Kyoto, Japan)	Monitoring MB and CR concentrations

3. Results and discussion

3.1. Characterization of the adsorbent

The successful compositing of UiO-66-NH_2 on the hydrochar was confirmed through X-ray diffraction (XRD) and diffuse reflectance infrared Fourier transform (DRIFT) spectroscopy. The XRD patterns, as shown in Fig. 1**b**, confirmed the successful synthesis of UiO-66-NH_2 with characteristic peaks at 2θ = 7.3°, 8.5°, and 25.7° (Reference code: 00–071-0285). The HTC sample exhibited characteristic carbon peaks at 2θ = 25.9° and 44.3° (Reference code: 04–015-2407). For determination of the crystallinity, curve-fitted XRD patterns were examined, which showed the degrees of crystallinity around 52 % and 60 % for UiO-66-NH_2($ZrCl_4$)@HTC and UiO-66-NH_2($ZrOCl_2$)@HTC, respectively. The DRIFT spectra revealed several characteristic peaks, as shown in Fig. 1**a**. The peaks at 658 cm^{-1} and 771 cm^{-1} correspond to the stretching vibrations of the Zr − O bond, confirming the presence of the MOF. The peak at 1261 cm^{-1} is attributed to the bending vibration of the N−H bond, and the peak at 1397 cm^{-1} is indicative of the benzene ring skeleton vibration (Hashem et al., 2019). Additionally, the peak at 1506 cm^{-1} corresponds to the C=C stretching in the aromatic ring, while the characteristic peaks at 3475 cm^{-1} are associated with the NH_2 group of the organic linker (Luu et al., 2015). The HTC sample spectra showed peaks at 3333 cm^{-1} (O–H stretching), 2899 cm^{-1} (C–H stretching), and 1023 cm^{-1} (C–O stretching vibrations) (Güdücü et al., 2021). Both XRD and DRIFT confirmed the successful incorporation of HTC without affecting the original MOF crystallinity.

The porosity characteristics of the materials, such as specific surface area and the proportion of micro- and mesopores, significantly influence their capacity to adsorb organic pollutants such as dyes. The surface area and pore structure of the adsorbents were evaluated using the Brunauer–Emmett–Teller (BET) method based on N_2 isotherms (Fig. 2). Although both materials displayed similar curves, UiO-66-NH_2($ZrOCl_2$)@HTC exhibited a more prominent hysteresis (between 0.3 and 0.99P/PO), suggesting a higher presence of mesopores in its pore structure. However, the curves indicate a high presence of micropores due to their high adsorbed amounts of N_2 at low partial pressures (Chen et al., 2015; Chen et al., 2023). Adsorbents with combined mesopores and micropores in their structure are highly suitable for organic molecule removal because both types of pores have significant and different roles concerning the efficient pollutant diffusion in the adsorbent's pore networks (Grimm et al., 2024). Table 3 shows that HTC exhibited a low BET surface area of 0.4 m^2/g and a minimal pore volume of 0.0004 cm^3/g, consisting mainly of mesopores (50 %), with contributions from micropores (25 %) and macropores (25 %). In contrast, UiO-66-NH_2($ZrCl_4$)@HTC and UiO-66-NH_2($ZrOCl_2$)@HTC showed significantly higher surface areas of 87.2 m^2/g and 62.6 m^2/g, respectively, confirming the successful incorporation of UiO-66-NH_2 onto HTC. The pore volumes of UiO-66-NH_2($ZrCl_4$)@HTC and UiO-66-NH_2($ZrOCl_2$)@HTC were 0.0448 cm^3/g and 0.0454 cm^3/g, respectively. UiO-66-NH_2($ZrCl_4$)@HTC had a higher proportion of micropores (56.7 %) compared to UiO-66-NH_2($ZrOCl_2$)@HTC (37 %), whereas the latter showed a higher mesopore content (59.3 % versus 40.6 % for the former). These observations underscore the mesoporous nature of both composites, which is critical for effective dye adsorption due to the sample surface area and pore volume available for interaction with dye molecules (Abdoul et al., 2023). The choice of zirconium precursor notably influenced the surface area and pore distribution: $ZrCl_4$ promoted more microporous structures, while $ZrOCl_2{\cdot}8H_2O$ favoured mesopore formation.

The morphology of the synthesized samples was further studied via FESEM and EFTEM images. The SEM images (Fig. 3**a, b**) depict octahedral microcrystals with particle sizes over the micrometre scale for UiO-66-NH_2. Further analysis using EFTEM characterization (Fig. 3**c, d**) showed that the samples maintained their octahedral and porous

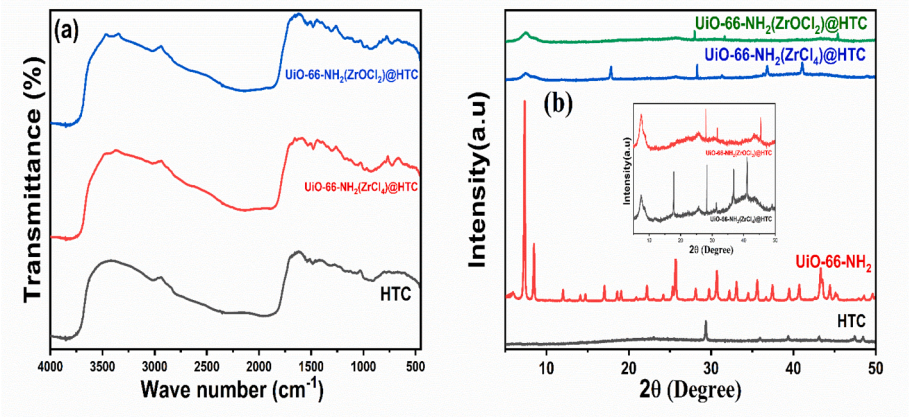

Fig. 1. (a) DRIFT spectra of HTC, UiO-66-NH_2($ZrCl_4$)@HTC, and UiO-66-NH_2($ZrOCl_2$)@HTC. **(b)** XRD patterns of HTC, UiO-66-NH_2, UiO-66-NH_2($ZrCl_4$)@HTC, and UiO-66-NH_2($ZrOCl_2$)@HTC.

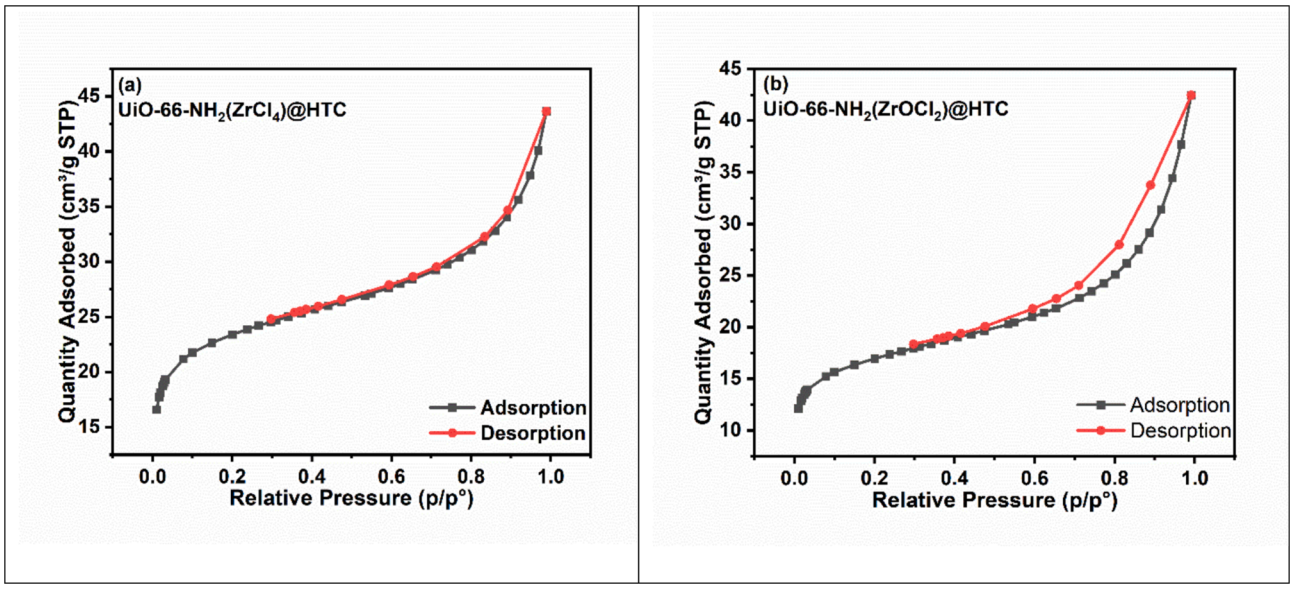

Fig. 2. N_2 adsorption–desorption isotherm plot of **(a)** UiO-66-NH_2($ZrCl_4$)@HTC and **(b)** UiO-66-NH_2($ZrOCl_2$)@HTC.

Table 3
BET Surface area and pore characteristics of the adsorbents.

Adsorbents	Surface area (m^2/g)	Pore diameter (nm)	Pore Volume (cm^3/g)	Micro pores %	Meso pores%	Macro pores%
HTC	0.4 ± 0.02	1.4 ± 0.1	0.0004	25 ± 2	50 ± 2	25 ± 1
UiO-66-NH_2($ZrCl_4$)@HTC	87.2 ± 1.7	2.7 ± 0.1	0.0448	56.7 ± 0.4	40.6 ± 0.4	2.7 ± 0.1
UiO-66-NH_2($ZrOCl_2$)@HTC	62.6 ± 1.2	3.5 ± 0.2	0.0454	37 ± 0.5	59.3 ± 0.5	3.7 ± 0.1

structures (Chen et al., 2023). The uniform size distribution of the MOF nanoparticles, with diameters ranging from 10 to 20 nm, was achieved due to the mechanical stirring of the growth solution under solvothermal conditions (El-Mehalmey et al., 2018). Additionally, energy-dispersive X-ray spectroscopy (EDX) supports the uniform loading of the MOF onto the carbon support. As depicted in Fig. 3**e, f**, the EDX maps for C, O, N, Cl, and Zr revealed a consistent pattern that aligned with the composite map of the carbon support, indicating homogeneous MOF distribution.

Further elemental characterization was conducted through XPS to examine the surface features and composition of the UiO-66-NH_2@HTC samples synthesized using different precursors. Additionally, the XPS analysis was used to assess the samples after the adsorption of MB and CR dyes. As shown in Fig. 4, characteristic peaks attributed to UiO-66-NH_2, such as C 1 s (C-C at 284.6–284.7 eV), N 1 s (C-NH_2 at 399.6 eV), O 1 s (O-C=O at 531.9 eV), O 1 s (C-O at 533.2 eV), and Zr 3d (Zr^{+4} at 185.3–185.4 eV), remained consistent across all samples (El-Mehalmey et al., 2018; Cheng et al., 2022; Hegde et al., 2023). Additionally, after MB adsorption, new peaks appeared, including heterocyclic nitrogen (N from the MB phenothiazine ring) at 401.0 eV (Thomas, 1996) and tertiary amine nitrogen ($N(CH_3)_2$) at 399.2 eV (Meng et al., 2024), along with sulfonate oxygen (O=S=O) at 533.4 eV. Similarly, after CR adsorption, additional peaks emerged, notably from the dye's sulfonate groups (S 2p at 167.3 eV) (Adams et al., 2009) and azo groups (N=N at 400.2 eV) (Olchowski et al., 2021). These findings emphasize the effective adsorption of both dyes onto the UiO-66-NH_2@HTC framework.

3.2. Optimizing dye adsorption on UiO-66-NH_2@HTC Composites: Influence of pH, Time, and initial dye concentration

The adsorption performance of UiO-66-NH_2@HTC composites was analysed across a pH range from 3 to 9, with contact times from 1 h to 24 h and initial dye concentrations from 25 mg/L to 700 mg/L. The primary objective was to modify the surface of UiO-66-NH_2 to expose either a positive or negative charge, thereby enhancing its affinity towards specific dyes. This goal was successfully achieved, as demonstrated by the distinct adsorption behaviours of the cationic dye MB and the anionic dye CR. As shown in Fig. 5**a**, MB exhibited significantly better adsorption capacity on the negatively charged surface of UiO-66-NH_2@HTC for both $ZrCl_4$ and $ZrOCl_2{\cdot}8H_2O$ precursors. Conversely, CR showed superior adsorption capacity on the positively charged surface of UiO-66-NH_2@HTC for both precursors (Fig. 5**b**). It is evident that when the surface is negatively charged, MB adsorption is favoured, while positively charged surfaces favour CR adsorption. The relatively high adsorption capacity observed for HTC indicates that its surface is also negatively charged, although the lower specific surface area of HTC compared to the UiO-66-NH_2 composites accounts for its reduced overall adsorption capacity. These findings clearly indicate that surface charge modification of UiO-66-NH_2 effectively enhances selective dye adsorption, with negatively charged surfaces favouring cationic dyes and positively charged surfaces favouring anionic dyes (Cheng et al., 2022). Regarding contact time, as illustrated in Fig. 5**c, d**, the adsorption dynamics differed significantly between MB and CR dyes. For MB dye, the alkali-activated UiO-66-NH_2 samples achieved 98 % adsorption removal within the first 2 h. In contrast, the acidic-activated samples reached the same removal percentage after 5 h for UiO-66-NH_2 prepared with the $ZrOCl_2$ precursor, and only about 80 % for UiO-66-NH_2 prepared with the $ZrCl_4$ precursor after 24 h. For CR dye, the acidic-activated UiO-66-NH_2 showed about 90 % removal within 24 h, whereas the alkali-activated samples achieved a removal range of 68–75 % in the same period. The superior performance of UiO-66-NH_2 using the $ZrOCl_2{\cdot}8H_2O$ precursor compared to UiO-66-NH_2 using $ZrCl_4$ can be attributed to factors beyond molecular charge and static charge, such as specific surface areas, pore size distributions, and the size of pollutant molecules. By preparing UiO-66-NH_2 with two different

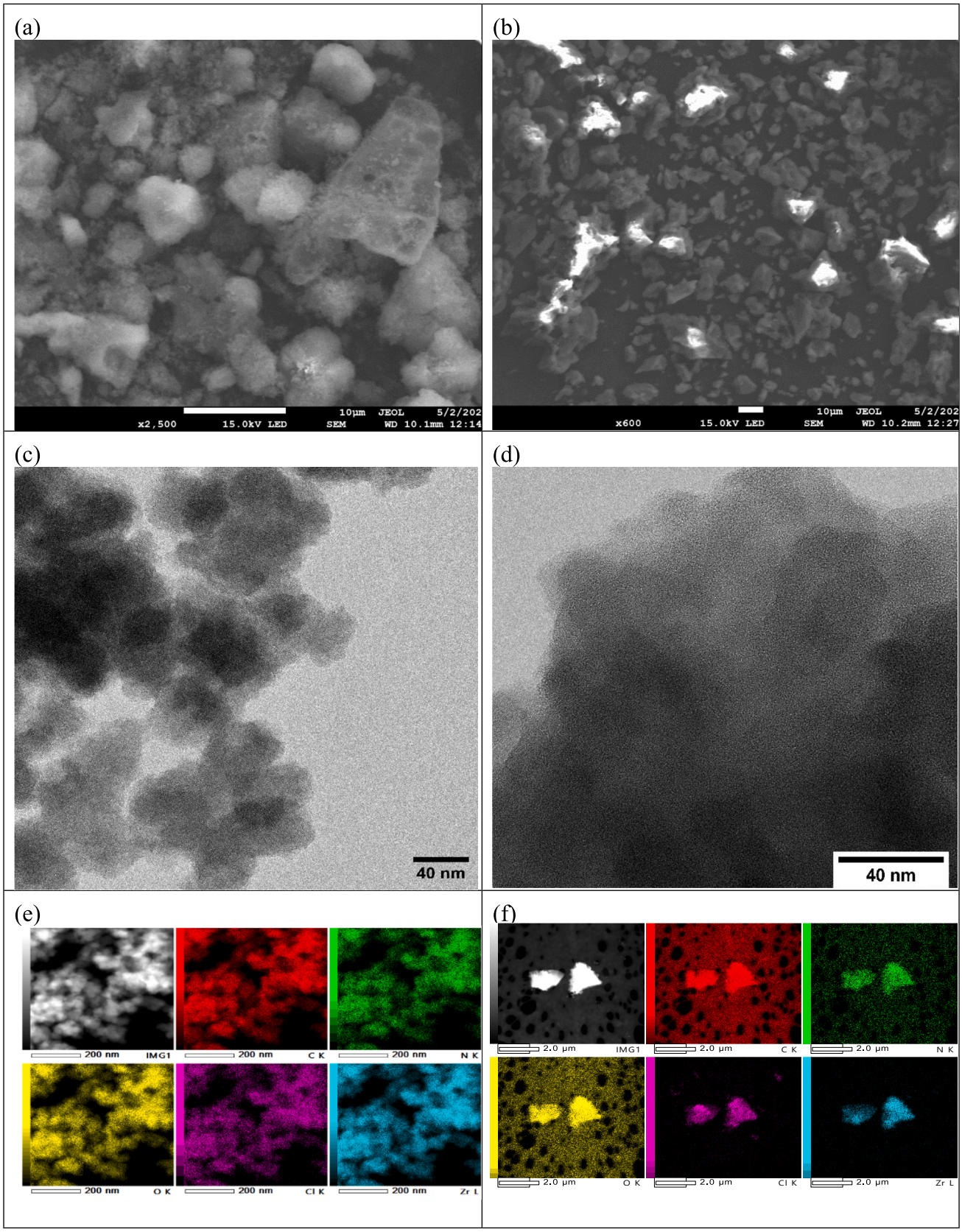

Fig. 3. (a, b) FESEM images; (c, d) EF-TEM images; (e, f) EDX mapping images of UiO-66-NH_2($ZrCl_4$)@HTC and UiO-66-NH_2($ZrOCl_2$)@HTC, respectively.

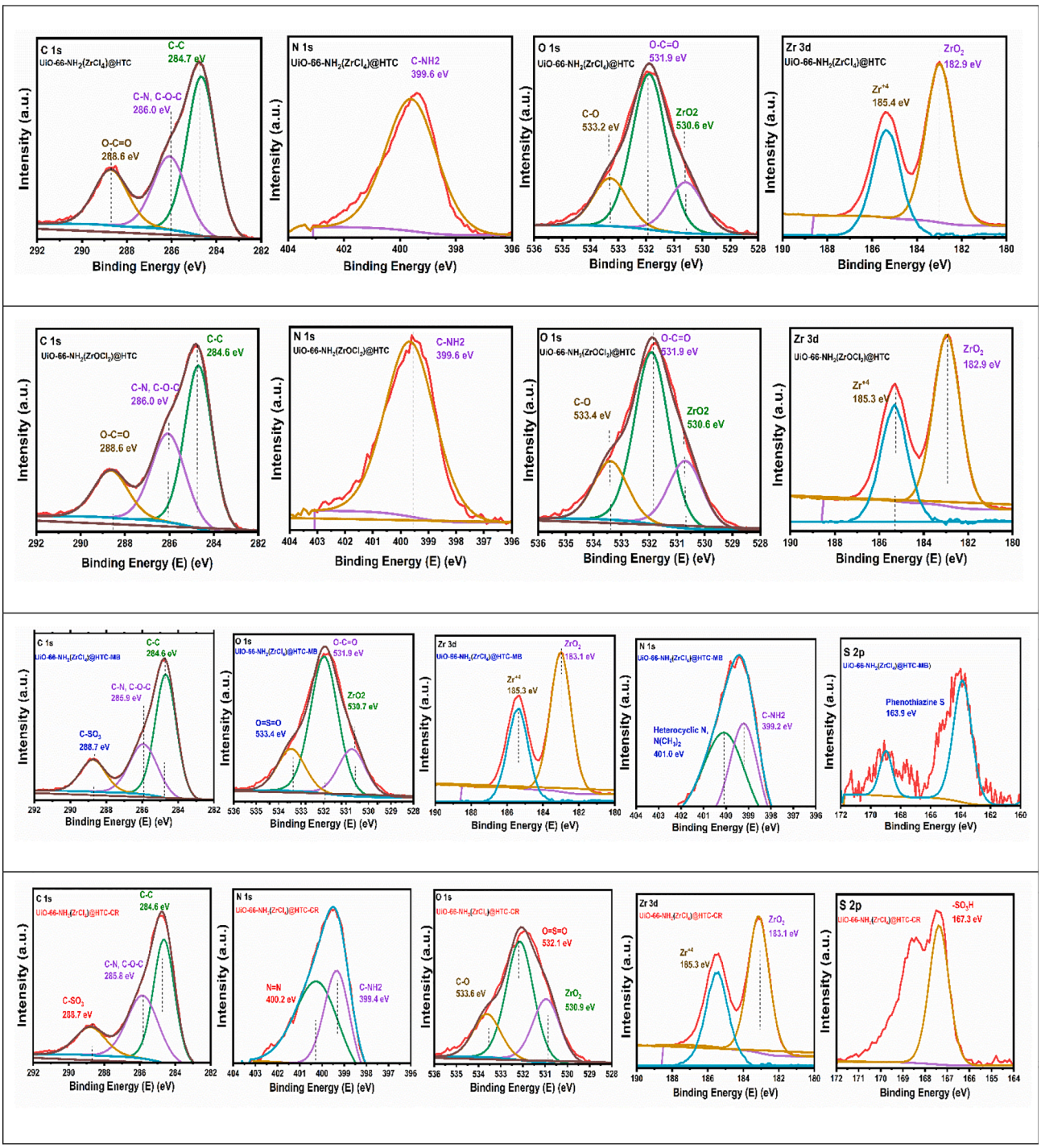

Fig. 4. XPS analysis, first and second rows: UiO-66-NH_2($ZrCl_4$)@HTC and UiO-66-NH_2($ZrOCl_2$)@HTC before adsorption; Third row: UiO-66-NH_2@HTC after MB adsorption; Bottom row:UiO-66-NH_2@HTCafterCRadsorption.

precursors, $ZrCl_4$ and $ZrOCl_2{\cdot}8H_2O$, we were able to highlight the critical role of pore size distribution in determining dye adsorption efficiency. A diverse pore size distribution enhances the adsorption capacity of materials by allowing larger pores to accommodate larger dye molecules, while smaller pores effectively capture smaller molecules. This combination broadens the range of adsorption, making the material more versatile in adsorbing dyes of different molecular sizes. The presence of mesopores, as revealed by BET analysis, in the UiO-66-NH_2@HTC composite prepared using $ZrOCl_2{\cdot}8H_2O$ facilitated more efficient adsorption of larger dye molecules, underscoring the importance of tailoring pore structures to the specific sizes and characteristics of the target pollutants (Ighalo et al., 2021; Wen et al., 2020). Additionally, the adsorption behaviour of MB and CR dyes was investigated over a concentration range of 25 mg/L to 550 mg/L at room temperature (Fig. 4**f and 5**). The removal efficiency was notably higher at lower initial concentrations (25–200 mg/L), attributed to the larger number of vacant active sites available for adsorption. However, as the initial concentration exceeded 250 mg/L, the removal efficiency declined due to the saturation of the active sites. Notably, [UiO-66-NH2($ZrOCl_2$)]$^-$@HTC and [UiO-66-NH_2($ZrCl_4$)]$^+$@HTC showed superior results for MB and CR, respectively, compared to other samples. This finding aligns with the effective acidic or basic activation of UiO-66-

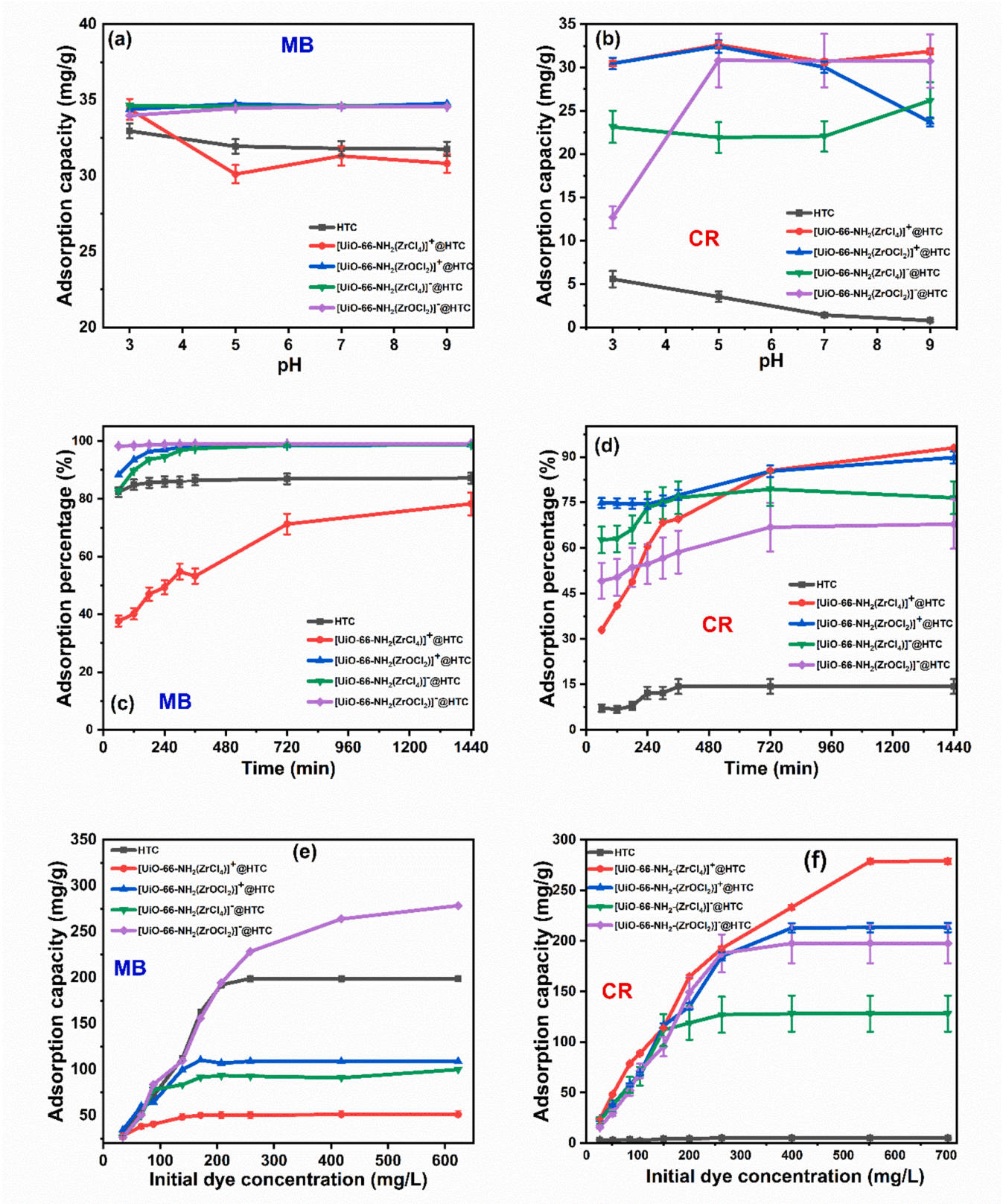

Fig. 5. Optimization of adsorption showing the effect of pH (a, b); time (c, d); and initial dye concentration (e, f) on MB and CR adsorption for HTC, [UiO-66-$NH_2(ZrCl_4)]^+$@HTC, [UiO-66-$NH_2(ZrOCl_2)]^+$@HTC, [UiO-66-$NH_2(ZrCl_4)]^-$@HTC, and [UiO-66-$NH_2(ZrOCl_2)]^-$@HTC.

NH_2, enhancing its adsorption performance for specific dyes.

3.3. Kinetics studies

To explore the adsorption rate, we applied various kinetic models. These models describe the relationship between adsorption parameters and time. The equations for the pseudo-first-order and pseudo-second-order models are provided below (Hegazy et al., 2024):

Pseudo-First-Order model (Eq. (3)

$$\log(q_e - q_t) = \log q_e - \left(\frac{K_1 t}{2.303}\right) \tag{3}$$

Pseudo-Second-Order model (Eq. (4)

$$\frac{t}{q_t} = \frac{1}{K_2 q_e^2} + \frac{t}{q_e} \tag{4}$$

In these equations, q_t represents the adsorption capacity at time t, q_e is the equilibrium adsorption capacity, K_1 and K_2 are the respective rate constants. Additionally, the Weber–Morris intra-particle diffusion model was considered:

Weber–Morris intra-particle diffusion model (Eq. (5)

$$q_t = K_i t^{\frac{1}{2}} + c \tag{5}$$

Here, c is a constant related to diffusion resistance while K_i represents the intra-particle diffusion rate constant.

The findings showed that the pseudo-second-order kinetic model most accurately represented the experimental data, with an average R^2 of 0.99, fitting the data better than the pseudo-first-order model, which had an average R^2 of 0.945, as shown in Fig. 6**a–d**. The pseudo-second-order model assumes that chemisorption is the main adsorption mechanism, indicating strong interactions between MB, CR, and the active

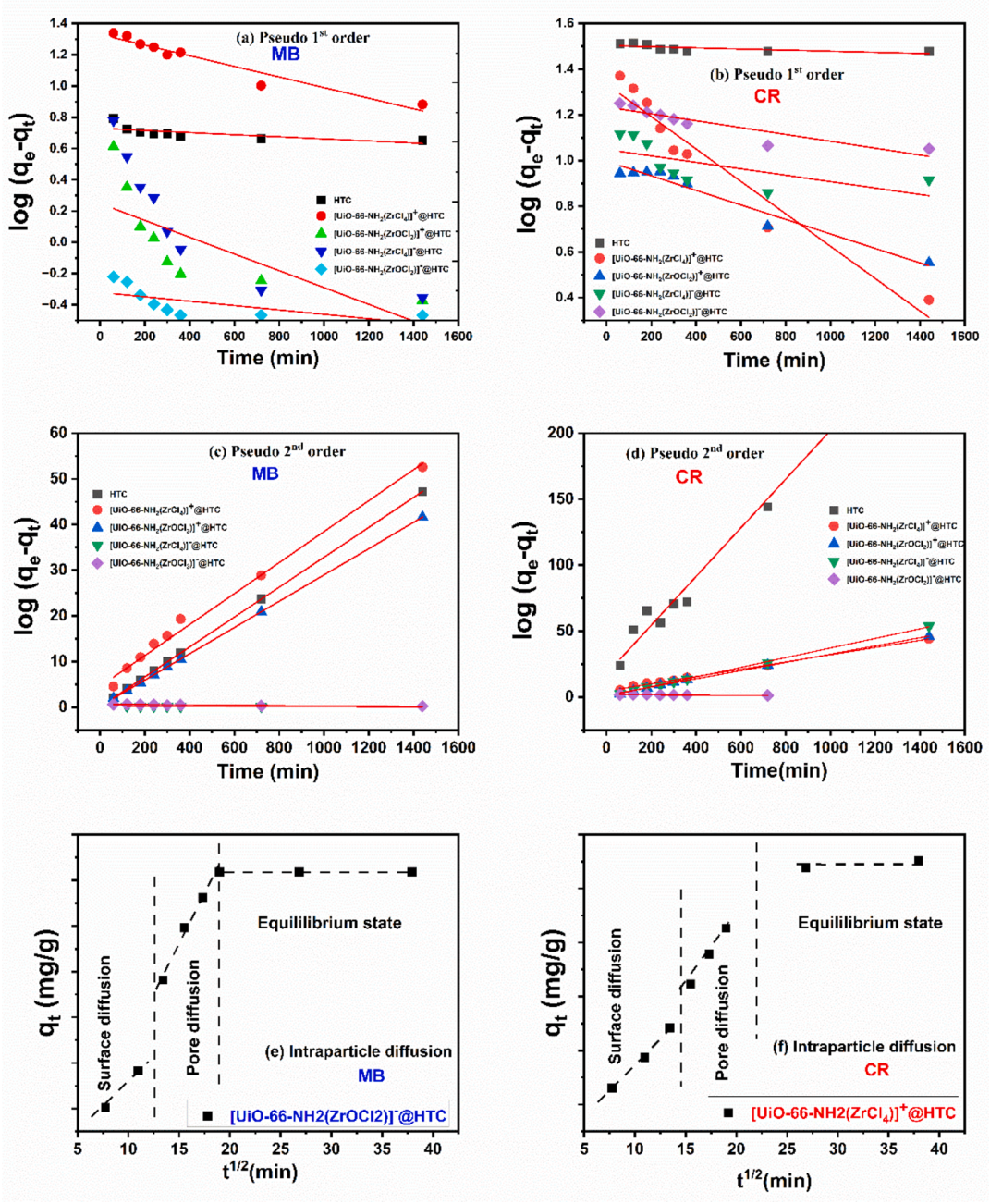

Fig. 6. Linear plots for Pseudo 1st order (a, b); Pseudo 2nd order (c, d); and Intraparticle diffusion kinetics (e, f) on MB and CR adsorption.

sites in UiO-66, involving the exchange or sharing of electrons via covalent forces and ion exchange (Du et al., 2021). Table 4 shows the adsorption rate constants k_1 and k_2 for the pseudo-first-order and pseudo-second-order models, respectively. For MB adsorption, the k_2 value for UiO-66-NH_2 prepared from $ZrOCl_2{\cdot}8H_2O$ was significantly higher (6.60 g/mg·min) compared to the sample prepared from $ZrCl_4$ (0.77 g/mg·min). Similarly, for CR adsorption, UiO-66-NH_2 prepared from $ZrOCl_2{\cdot}8H_2O$ exhibited a higher k_2 value (0.75 g/mg·min) compared to the sample prepared from $ZrCl_4$ (0.28 g/mg·min). This can be attributed to the higher diffusion rate of dye molecules into the mesopores of samples prepared from $ZrOCl_2{\cdot}8H_2O$ compared to the micropores in samples prepared from $ZrCl_4$ (Feil et al., 2012; Al Amery et al., 2020). Additionally, the calculated q_e values for the five different adsorbents closely aligned with the experimental q_e values, further supporting the model's accuracy in describing the adsorption process. To further investigate the adsorption mechanism and the factors influencing kinetics, the Weber–Morris intra-particle diffusion model was utilized, as shown in Fig. 5**f and 6e**. The data indicated three distinct stages of linearity for the adsorption of MB and CR. The initial phase (15–90 min) corresponded to external surface diffusion, where adsorbate molecules moved from the bulk solution to the adsorbent surface. The second phase, lasting approximately 300 min, was attributed to pore diffusion, which was the rate-limiting step. The third phase marked the equilibrium stage. In the case of UiO-66-NH_2($ZrOCl_2$)@HTC, the initial step (film diffusion) closely resembled the second step (pore diffusion), likely due to the presence of many oxygen-containing functional groups, indicating significant surface diffusion involvement (Kumar Prajapati and Kumar Mondal, 2022). Moreover, the curve's deviation from the coordinate origin suggested that intra-particle diffusion was not the only factor influencing the adsorption rate, suggesting that multiple mechanisms were involved (Han et al., 2021).

3.4. Adsorption isotherms

To better understand the interactions between the adsorbate and the adsorbent, the experimental equilibrium data were analysed by using two widely recognized models:

Langmuir Isotherm: The Langmuir isotherm model postulates that adsorbate molecules create a monolayer on the surface of the adsorbent, without considering steric hindrances between adjacent active sites (Pandey et al., 2024). It is commonly employed for chemisorption processes and can be expressed as follows:

$$\frac{C_e}{q_e} = \frac{1}{bqm} + \frac{C_e}{qm} \tag{6}$$

where q_m represents the maximum adsorption capacity (mg/g), and b stands for the Langmuir constant (L/mg). The values of q_m and b were obtained by calculating the linear plot between C_e/q_e and C_e, as shown in Fig. 7**a, b.**

Freundlich Isotherm: The Freundlich isotherm model proposes that adsorbate molecules form multilayers on the surface of the adsorbent, indicating the energetic heterogeneity of the adsorbent's surface (Hegazy and Mohamed, 2021). The linear equation for this model is as follows:

$$\log q_e = log\mathrm{Kf} + \frac{1}{n}\log C_e \tag{7}$$

In this equation, K_f represents the Freundlich constant [mg g^{-1} (mg L^{-1}) n], while 1/n is a dimensionless parameter. Plotting log(q_e) against log (C_e) enables the determination of the K_f and 1/n constants, as shown in Fig. 7**c, d.**

The analysis of the experimental equilibrium data, as presented in Fig. 7 and Table 5, highlights the suitability of isotherm models for characterizing the adsorption process. The Langmuir model exhibited a superior fit, with higher R^2 values compared to the Freundlich model, indicating a monolayer distribution of the dye and the presence of homogeneous active sites on the surface of the adsorbents (Huang et al., 2022). For MB adsorption, the negatively charged surface samples exhibited significantly higher q_m values compared to the positively charged surface samples, emphasizing that electrostatic attraction plays a crucial role between the dye molecules and the adsorbent surface. Specifically, [UiO-66-NH_2($ZrOCl_2$)]$^-$@HTC achieved a q_m of 263.1 mg/g, while [UiO-66-NH_2($ZrCl_4$)]$^-$@HTC achieved only 91.74 mg/g. Conversely, for CR adsorption, the positively charged surface samples showed superior performance, with [UiO-66-NH_2($ZrOCl_2$)]$^+$@HTC exhibiting a q_m of 277.77 mg/g, compared to 263.15 mg/g for [UiO-66-NH_2($ZrCl_4$)]$^+$@HTC. Furthermore, the samples prepared using the $ZrOCl_2{\cdot}8H_2O$ precursor consistently demonstrated higher q_m values than those prepared using $ZrCl_4$, regardless of the dye. For CR adsorption, [UiO-66-NH_2($ZrOCl_2$)]$^+$@HTC showed a q_m of 277.77 mg/g, versus 263.15 mg/g for [UiO-66-NH_2($ZrCl_4$)]$^+$@HTC. Similarly, for MB adsorption, [UiO-66-NH_2($ZrOCl_2$)]$^-$@HTC had a q_m of 263.1 mg/g, significantly higher than the 91.74 mg/g observed for [UiO-66-NH_2($ZrCl_4$)]$^-$@HTC. These findings suggest that the mesoporous structure and enhanced crystallinity of UiO-66-NH_2 prepared using the $ZrOCl_2{\cdot}8H_2O$ precursor contribute to improved adsorption efficiency due to better diffusion and increased availability of active sites. Notably, the maximum adsorption capacities (q_m) for this work stand at 263.1 mg/g and 277.77 mg/g for MB and CR, respectively, surpassing the capacities of other reported adsorbents (Table 6) (Gómez-Avilés et al., 2023; Timofeev et al., 2023; Cheng et al., 2022; Fan et al., 2023; Zhang et al., 2019; Kang et al., 2024; Abas and Fathy, 2024; Liu et al., 2021; Mahmud et al., 2023; Yusop et al., 2023; Mousavi et al., 2021). It is evident from Table 6 that the adsorption capacity of synthesized MOFs is quite comparable with other available adsorbents. This significant result emphasizes the efficacy of modifying the surface charge and carefully selecting the precursor.

3.5. Thermodynamics analysis

To gain insights into the thermodynamic behaviour of the adsorption process, key parameters such as changes in enthalpy (ΔH^0), entropy (ΔS^0), and Gibbs energy (ΔG^0) were determined to evaluate the nature of the MB and CR adsorption on the prepared materials in terms of spontaneity, feasibility, randomness, exothermicity, or endothermicity. The ΔH^0, ΔS^0, and ΔG^0 are calculated from the experimental data collected across a range of temperatures, specifically at 283 K, 295 K, 308 K, and 318 K. The distribution coefficient, K_d, was computed using the following equation:

Table 4
Kinetic parameters for the adsorption of MB and CR.

Adsorbents	Pseudo 1st order				Pseudo 2nd order			
	q_e exp (mg/g)	q_e cal (mg/g)	k_1 (min^{-1})	R^2	q_e exp (mg/g)	q_e cal (mg/g)	k_2 (g/mg.min)	R^2
HTC	4.99	4.49	−0.05	0.49	4.99	5.42	0.007	0.98
[UiO-66-NH_2($ZrCl_4$)]$^+$@HTC(CR dye)	32.54	3.79	−1.6	0.94	32.54	36.36	0.28	0.99
[UiO-66 –NH_2($ZrOCl_2$)]$^+$@HTC (CR dye)	31.44	2.71	−0.69	0.95	31.44	32.05	0.75	0.99
[UiO-66-NH_2($ZrCl_4$)]$^-$@HTC (MB dye)	34.55	1.60	1.61	0.67	34.55	28.49	0.77	1
[UiO-66-NH_2($ZrOCl_2$)]$^-$@HTC(MB dye)	34.65	1.37	0.23	0.42	34.65	32.25	6.60	0.86

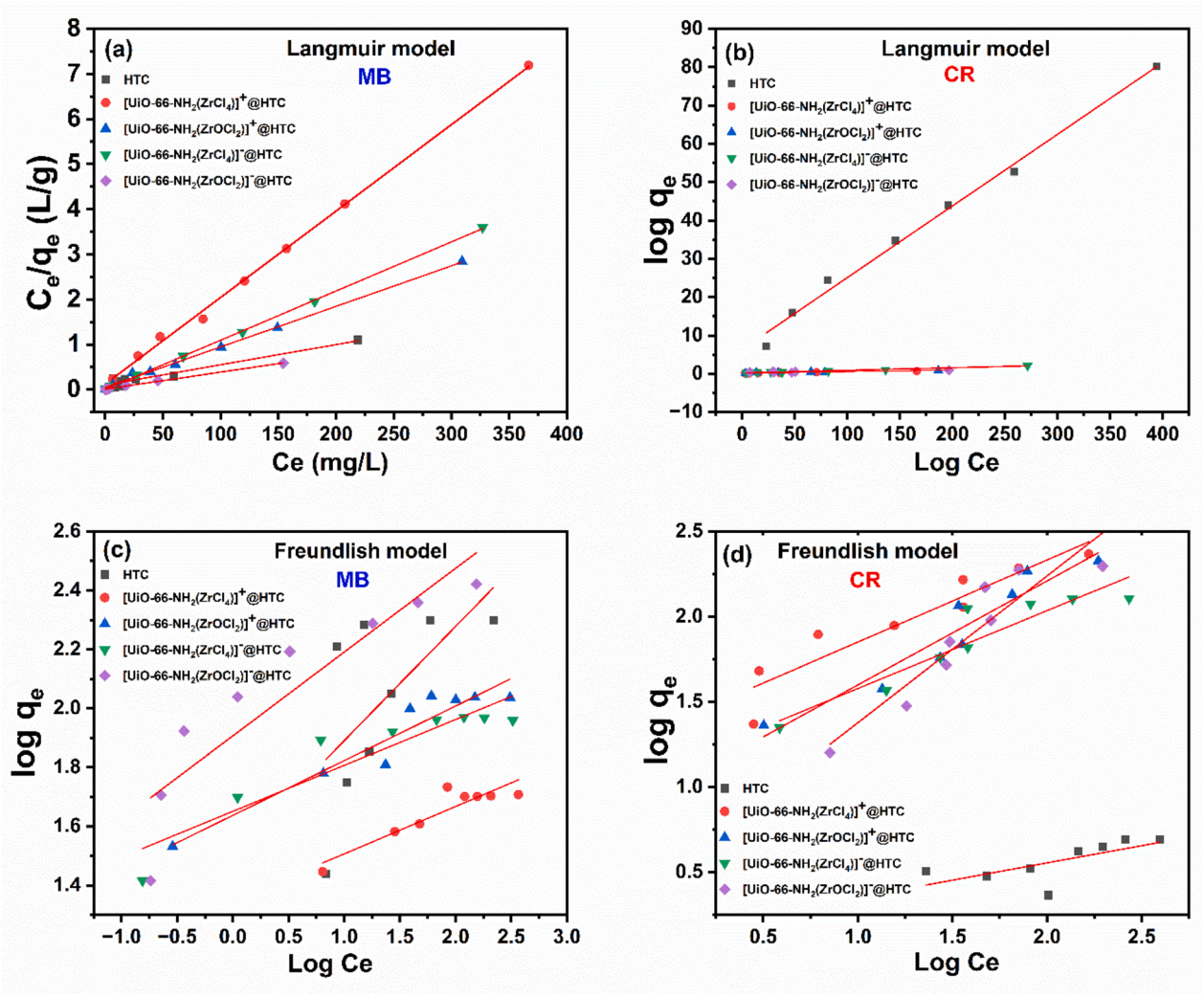

Fig. 7. Adsorption isothermal models for MB dye and CR dye adsorption **(a, b)** Langmuir isotherm; **(c, d)** Freundlich isotherm.

Table 5
Langmuir and Freundlich isotherms parameters.

Adsorbent	Langmuir model			Freundlich model		
	q_m (mg/g)	b (L/mg)	R^2	K_f [mg.g^{-1} (mg. L^{-1})^n]	1/n	R^2
HTC	5.34	0.029	0.993	1.16	0.203	0.489
[UiO-66-NH_2($ZrCl_4$)]$^+$@HTC (CR dye)	263.15	0.039	0.963	3.93	0.481	0.878
[UiO-66-NH_2($ZrOCl_2$)]$^+$@HTC (CR dye)	277.77	0.017	0.923	2.68	0.610	0.909
[UiO-66-NH_2($ZrCl_4$)]$^-$@HTC (MB dye)	91.74	0.23	0.999	6.22	0.076	0.789
[UiO-66-NH_2($ZrOCl_2$)]$^-$@HTC (MB dye)	263.1	0.79	0.997	6.73	0.283	0.827

$$Kd = \frac{q_e}{c_e} \tag{8}$$

The thermodynamic functions were assessed through the following relationships:

$$\ln Kd = \frac{\Delta S^\circ}{R} - \frac{\Delta H^\circ}{RT} \tag{9}$$

$$\Delta G^\circ = -RT\ln Kd \tag{10}$$

Here, T and R represent the temperature in Kelvin (K) and universal gas constant, respectively. The values of ΔH^0 and ΔS^0 were determined by plotting ln K_d against 1/T, as shown in Fig. 8**a, b**, with ΔH^0 corresponding to the slope and ΔS^0 to the intercept while ΔG^0 was calculated using Eq. (10).

The thermodynamic parameters obtained from this analysis are summarized in Table 7. The high R^2 values from the linear regression suggest a robust fit for the data. The signs of ΔH^0 and ΔS^0 indicate an endothermic process leading to an increase in disorder, reflecting the dynamic nature of the adsorption mechanism, and the ΔH^0 magnitude is consistent with a physical adsorption process. ΔG^0 indicates the spontaneity of the adsorption process (Ngobeni and Mulaba-Bafubiandi, 2023), and its negative values suggest that the process is spontaneous and favourable, whereas a positive value suggests that the process is unfavourable and nonspontaneous (Salmani Nuri et al., 2019).

3.6. *Proposed mechanism for the adsorption of MB and CR dyes*

The adsorption mechanism of MB and CR onto UiO-66-NH_2@HTC composites, as illustrated in Fig. 9, involves both physical attractions

Table 6
Comparative study on the effect of activation on UiO-66-based adsorbents and the maximum adsorption capacity of MB and CR by various adsorbent.

Adsorbent	Activation type/activator	Effect of activation	MB q_m (mg/g)	CR q_m (mg/g)	Refs
UiO-66-NH_2	N-cycloalkyl functionalization	Enhanced the structural stability, photocatalytic efficiency	–-	–-	(Gómez-Avilés et al., 2023)
UiO–66–NH_2	Aminoterephthalate	Increased basic sites, decrease surface area and micropores	–-	–-	(Timofeev et al., 2023)
UIO-66-NO_2	–NO_2/–NH_2	Introduction of functional groups	198	153	(Cheng et al., 2022)
UiO-66-PAMPS	Ionic polymer	Enhanced dispersibility, active Binding Sites	120.34	–-	(Fan et al., 2023)
ZIF-8-loaded UiO-66-NH_2	Acid activation with HCl	Increase Zeta Potential	173	–-	(Zhang et al., 2019)
UiO–66–NH_2	HCl,Ionic Liquid	Improved microporous structure and selectivity	–-	–-	(Kang et al., 2024)
Zeolite compounds	–-	–-	181.82	184.8	(Abas and Fathy, 2024; Liu et al., 2021)
Activated carbon	–-	–-	196.08	129.87	(Mahmud et al., 2023), 2023.; Yusop et al., 2023)
UiO–66–NH_2	Thermal, Solvent, and chemical	Thermal: increased porosity; solvent: removal of trapped molecules; chemical: introduction of function groups	200	–-	(Mousavi et al., 2021)
UiO-66-NH_2@HTC	Acid and basic activation with HCl, NaOH Chemical: $ZrCl_4$, $ZrOCl_2{\cdot}8H_2O$	Controlling surface charge, textural properties, and crystallinity	263.1	277.77	This work

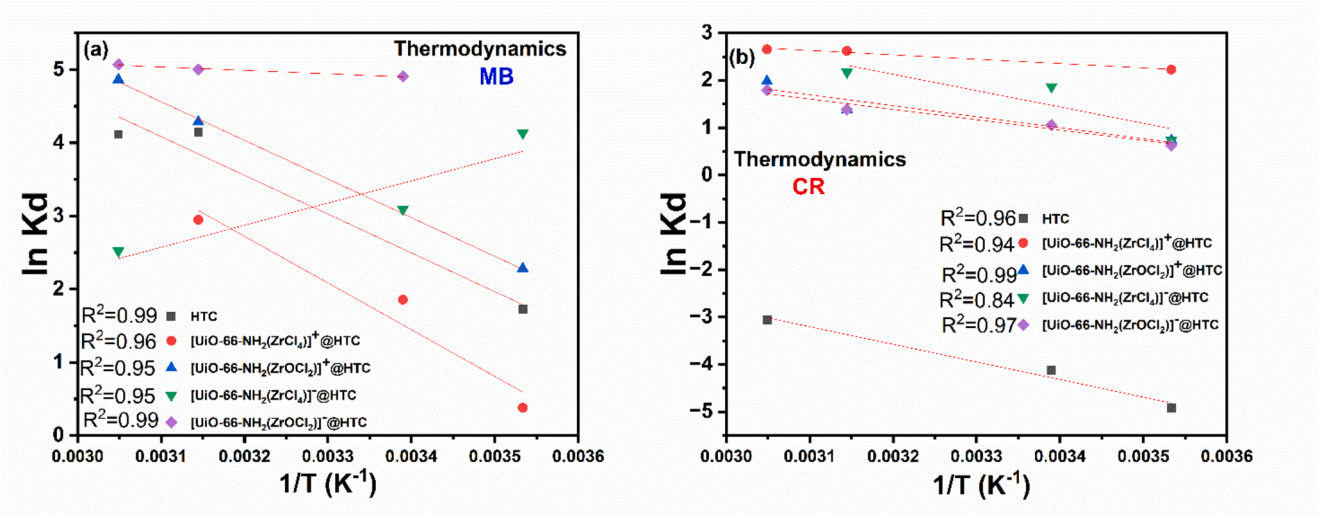

Fig. 8. The thermodynamic functions for (a) MB dye, (b) CR dye.

Table 7
The thermodynamic parameters for MB adsorption.

Adsorbent	ΔH^0 (kJ/mol)	ΔS^0 (J/mol/K)	ΔG^0 (kJ/mol) at temperatures			
			298 K	308 K	318 K	328 K
HTC (CR dye)	45.421	113.095	12.077	10.551	8.069	8.341
[UiO-66-NH_2($ZrCl_4$)]$^+$@HTC (CR dye)	10.996	55.928	−5.464	−5.835	−6.933	−7.240
[UiO-66 –NH_2($ZrOCl_2$)]$^+$@HTC (CR dye)	28.820	103.434	−1.797	−4.483	−3.665	−5.405
[UiO-66-NH_2($ZrCl_4$)]$^-$@HTC (MB dye)	0.002	0.0199	−10.244	−7.920	−9.510	−6.879
[UiO-66-NH_2($ZrOCl_2$)]$^-$@HTC (MB dye)	3.918	54.030	−14.208	−12.562	−13.220	−13.835

and chemical interactions. For physical adsorption processes, electrostatic attractions play a significant role (Han et al., 2021; Zhang et al., 2019). For MB, a cationic dye is attracted to the negatively charged surface of the UiO-66-NH_2@HTC composites, particularly those activated with a basic treatment. This negative charge arises because, in a basic environment, the amino groups (–NH_2) in UiO-66-NH_2 undergo deprotonation, forming negatively charged amide ions ($-NH^-$): $-NH_2 + OH^- \rightarrow -NH^- + H_2O$. Conversely, CR, an anionic dye, is effectively adsorbed by the positively charged surface of the composites activated with acidic treatment. The amine groups (–NH_2) in UiO-66-NH_2 are protonated in an acidic environment, converting them to ammonium group ions ($-NH_3^+$): $-NH_2 + H^+ \rightarrow -NH_3^+$. Hydrogen bonding further enhances adsorption capacity, as the amine groups facilitate bonding with functional groups of both dyes (Luu et al., 2015). Additionally, π–π stacking interactions between the aromatic structures of the dyes and the benzene rings in the UiO-66-NH_2 framework contribute to the adsorption process (Athari et al., 2022), while surface functional groups on the HTC, such as hydroxyl and carboxyl groups, also interact with the dye molecules (Yu et al., 2024). The chemical interactions are evidenced by XPS results, as shown in Fig. 4. Significant changes in the atomic percentages of carbon (C), oxygen (O), and nitrogen (N) after adsorption indicate the involvement of these elements in the adsorption process. Notably, sulphur (S) peaks appeared post-adsorption, corresponding to the sulphur content in both MB and CR dyes. For CR, the presence of the N=N double bond peak indicates its adsorption involvement, while for MB, the emergence of heterocyclic

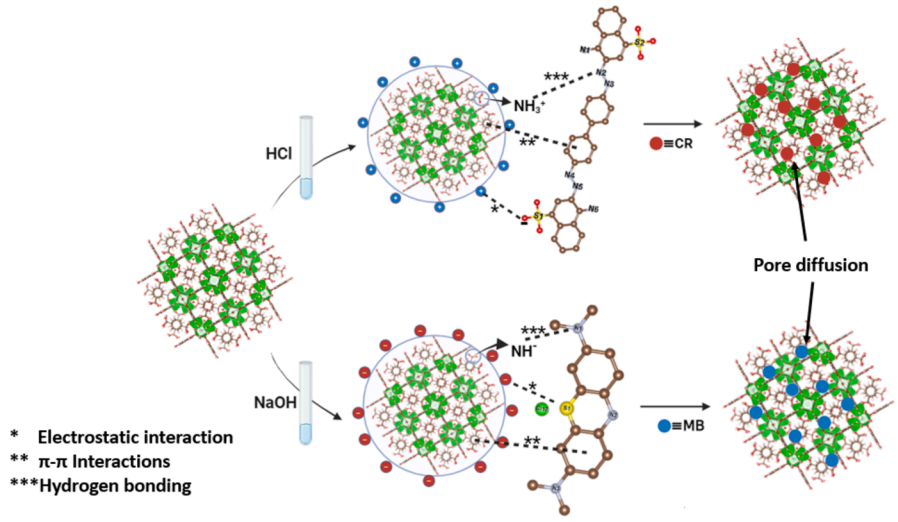

Fig. 9. Mechanism of the adsorption of MB and CR on UiO-66-NH_2@HTC.

nitrogen and $N(CH_3)_2$ peaks confirms its interaction with the composite surface (Cheng et al., 2022; Wang et al., 2022).The adsorption performance of the UiO-66-NH_2@HTC composites shows a complex relationship between pore size distribution and the adsorption of both dyes, which is evident in the experimental data. For the MB molecule (~1.4 nm) (Niu et al., 2018), the [UiO-66-NH_2($ZrOCl_2$)]@HTC composite, with its larger pore diameter of 3.5 nm and a higher mesopore content, exhibits superior adsorption capacity, particularly at higher dye concentrations. This suggests that the larger mesopores in [UiO-66-NH_2($ZrOCl_2$)]@HTC facilitate the effective diffusion and adsorption of smaller dye molecules. However, for the CR molecule (~2.0 nm) (Liu et al., 2019), the [UiO-66-NH_2($ZrCl_4$)]@HTC composite, which has a smaller pore diameter of 2.7 nm and more micropores, unexpectedly shows better adsorption performance, both in terms of adsorption percentage over time and adsorption capacity at varying concentrations. This suggests that factors like surface chemistry, charge distribution, and specific dye-adsorbent interactions play crucial roles in adsorption efficiency, beyond just pore size.

3.7. Regeneration Performance, Selectivity, and stability of activated UiO-66-NH_2@HTC

Regeneration of adsorbents is crucial for designing sustainable adsorption systems. In the regeneration tests, the activated UiO-66-NH_2@HTC composites showed excellent reusability for MB, maintaining over 96 % adsorption efficiency through four cycles before decreasing to 62.26 % in the fifth cycle. For CR, the adsorption capacity dropped significantly after the second cycle, reaching 7.84 % after the fifth cycle (Fig. 10a, b). This decline can be attributed to pore blockage, reducing the available active sites for adsorption (Yazdi et al., 2024).

To evaluate selectivity, experiments were conducted using a 40-ppm mixture of MB and CR. MB consistently exhibited higher removal efficiency compared to CR (Fig. 10**c**), likely due to its smaller molecular size, which facilitates better diffusion and adsorption within the pore structure. In contrast, the larger CR molecule encountered greater diffusion resistance, resulting in lower adsorption efficiency.

Stability tests were performed under acidic (pH 2), neutral (pH 7), and alkaline (pH 12) conditions. Minimal iron leaching was observed across all pH levels, with slightly higher leaching noted at pH 2. XPS analysis (Fig. 4) confirmed that there were no significant structural changes before and after adsorption, indicating the stability of the adsorbent under various conditions.

4. Conclusion

This study provides a comprehensive investigation into the synthesis, characterization, and application of UiO-66-NH_2@HTC composites. The choice of zirconium precursors, $ZrCl_4$ and $ZrOCl_2{\cdot}8H_2O$, significantly influenced the structural properties of UiO-66-NH_2@HTC, with $ZrCl_4$ promoting micropore formation and $ZrOCl_2{\cdot}8H_2O$ enhancing mesopore development. Acidic and basic treatments were effective in controlling the surface charge, thereby improving the adsorption capacity of the synthesized composites for various dyes. X-ray diffraction analysis revealed crystallinities of 51.7 % for UiO-66-NH_2($ZrCl_4$)@HTC and 60 % for UiO-66-NH_2($ZrOCl_2$)@HTC, underscoring their structural differences. Adsorption kinetics followed the pseudo-second-order model, emphasizing chemisorption as the primary mechanism, with higher adsorption rates observed for $ZrOCl_2{\cdot}8H_2O$-derived UiO-66-NH_2@HTC. The Langmuir model provided an excellent fit, highlighting monolayer adsorption behaviour and homogeneous active sites. The maximum adsorption capacities for MB and CR were determined as 263.1 mg/g and 277.77 mg/g, respectively, demonstrating the efficacy of UiO-66-NH_2@HTC composites in dye removal. The adsorption mechanism involved a combination of physical adsorption processes (electrostatic attraction, hydrogen bonding, π–π stacking, and pore diffusion) and chemical interactions, supported by XPS results. Moreover, the recyclability study indicated robust stability over multiple cycles, with MB maintaining over 96 % adsorption efficiency up to the fourth cycle. Conversely, CR exhibited decreased efficiency after the second cycle. Overall, this research underscores the potential of UiO-66-NH_2@HTC composites as effective adsorbents for wastewater treatment applications.

CRediT authorship contribution statement

Sherif Hegazy: Writing – original draft, Methodology, Investigation, Formal analysis, Data curation, Conceptualization. **Ayoub Ghannami:** Methodology, Data curation. **Glaydson S. dos Reis:** Methodology, Writing – review & editing. **Tao Hu:** Formal analysis. **Rachid Brahmi:** Writing – review & editing. **Sari Tuomikoski:** Writing – review & editing, Supervision, Resources. **Ulla Lassi:** Writing – review & editing, Supervision, Resources, Project administration. **Varsha Srivastava:** Writing – review & editing, Validation, Supervision.

Declaration of competing interest

The authors declare that they have no known competing financial

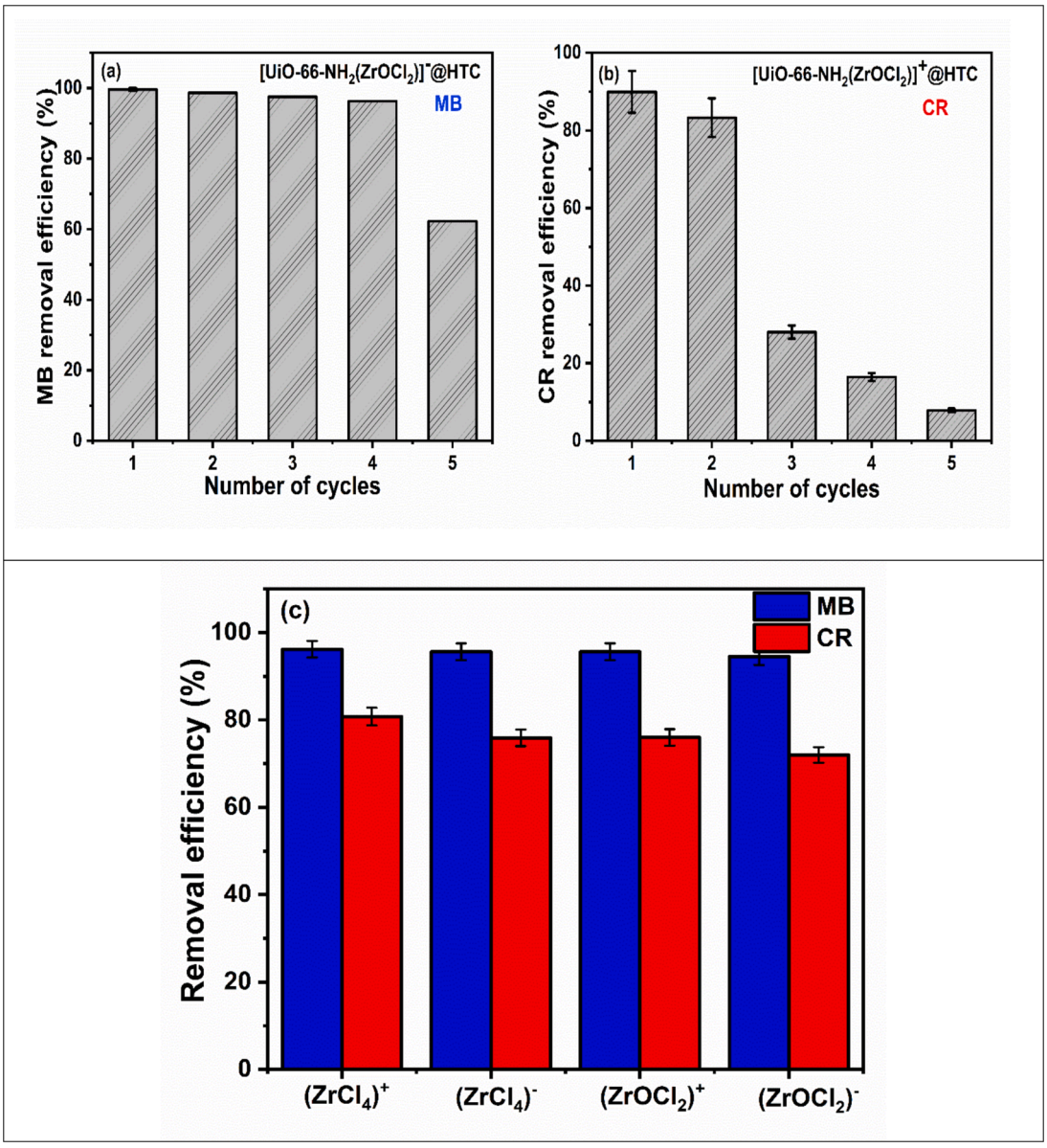

Fig. 10. Adsorption cycle performance of activated UiO-66-NH_2@HTC for (a) MB dye, (b) CR dye, (c) Selectivity test.

interests or personal relationships that could have appeared to influence the work reported in this paper.

The authors declare no conflict of interest. The first Author declares to use Chat GPT for ONLY checking and improving the English language for this manuscript and it is never used for generating or analyzing any results.

Data availability

The data presented in this study is available on request from the corresponding author.

Acknowledgments

Sherif Hegazy gratefully acknowledges Dr. Anne Heponiemi, Dr. Ahmed Hamdy, and Ms. Riikka Koski for their dedicated efforts and valuable contributions to this work. Dr. Glaydson Simoes dos Reis is thankful to the Research Council of Finland for the financial support. Bio4Energy - a Strategic Research Environment appointed by the Swedish government and the Swedish University of Agricultural Sciences are also acknowledged for the financial support.

References

Abas, K.M., Fathy, N.A., 2024. Sodalite zeolitic materials produced from coal fly ash for removal of congo red dye from aqueous solutions. Int. J. Environ. Sci. Technol. 21. https://doi.org/10.1007/s13762-023-05347-0.

Abdoul, H.J., Yi, M., Prieto, M., Yue, H., Ellis, G.J., Clark, J.H., Budarin, V.L., Shuttleworth, P.S., 2023. Efficient adsorption of bulky reactive dyes from water using sustainably-derived mesoporous carbons. Environ Res 221. https://doi.org/10.1016/j.envres.2023.115254.

Absalan, Y., Gholizadeh, M., Kim, E.B., Ameen, S., Wang, Y., Wang, Y., He, H., 2024. Recent progress on organic metal compound/MOF hybrids: From controllable synthesis to potential catalytic applications. Coord Chem Rev 515. https://doi.org/10.1016/j.ccr.2024.215972.

Adams, L., Oki, A., Grady, T., McWhinney, H., Luo, Z., 2009. Preparation and characterization of sulfonic acid-functionalized single-walled carbon nanotubes. Physica E Low Dimens Syst Nanostruct 41. https://doi.org/10.1016/j.physe.2008.11.018.

Ahmadijokani, F., Molavi, H., Rezakazemi, M., Tajahmadi, S., Bahi, A., Ko, F., Aminabhavi, T.M., Li, J.R., Arjmand, M., 2022. UiO-66 metal–organic frameworks in water treatment: A critical review. Prog Mater Sci 125. https://doi.org/10.1016/j.pmatsci.2021.100904.

Al Amery, N., Abid, H.R., Wang, S., Liu, S., 2020. Removal of methylene blue (MB) by bimetallic- metal organic framework. Journal of Applied Materials and Technology 2. https://doi.org/10.31258/jamt.2.1.36-49.

Athari, M., Fattahi, M., Khosravi-Nikou, M., Hajhariri, A., 2022. Adsorption of different anionic and cationic dyes by hybrid nanocomposites of carbon nanotube and graphene materials over UiO-66. Sci Rep 12. https://doi.org/10.1038/s41598-022-24891-2.

Ben Moussa, F., 2024. Physicochemical and Mechanical Properties of Metal-Organic Frameworks, in. ACS Symp. Ser. https://doi.org/10.1021/bk-2024-1463.ch002.

M. Cavali, N. Libardi Junior, J.D. de Sena, A.L. Woiciechowski, C.R. Soccol, P. Belli Filho, R. Bayard, H. Benbelkacem, A.B. de Castilhos Junior, A review on hydrothermal carbonization of potential biomass wastes, characterization and environmental applications of hydrochar, and biorefinery perspectives of the process, Science of the Total Environment 857 (2023). https://doi.org/10.1016/j.scitotenv.2022.159627.

Chaouiki, A., Fatimah, S., Chafiq, M., Ryu, J., Ko, Y.G., 2024. State-of-the-art advancements in metal−organic framework nanoarchitectures for catalytic applications. Appl Mater Today 38. https://doi.org/10.1016/j.apmt.2024.102224.

Chen, Q., He, Q., Lv, M., Xu, Y., Yang, H., Liu, X., Wei, F., 2015. Selective adsorption of cationic dyes by UiO-66-NH_2. Appl. Surf. Sci. 327, 77–85. https://doi.org/10.1016/j.apsusc.2014.11.103.

Chen, G., Liu, G., Pan, Y., Liu, G., Gu, X., Jin, W., Xu, N., 2023. Zeolites and metal-organic frameworks for gas separation: the possibility of translating adsorbents into membranes. Chem Soc Rev 52. https://doi.org/10.1039/d3cs00370a.

Chen, X., Wang, X., Liu, W., Tian, H., Du, Y., Wei, H., Tang, L., 2023. UiO-66 derived ZrO_2@C catalysts for the double-bond isomerization reaction of 2-butene. RSC Adv 13. https://doi.org/10.1039/d3ra01849k.

Cheng, S., Xie, P., Yu, Z., Gu, R., Su, Y., 2022. Enhanced adsorption performance of UiO-66 via modification with functional groups and integration into hydrogels. Environ Res 212. https://doi.org/10.1016/j.envres.2022.113354.

Cox, C.S., Slavich, E., Macreadie, L.K., McKemmish, L.K., Lessio, M., 2023. Understanding the Role of Synthetic Parameters in the Defect Engineering of UiO-66: A Review and Meta-analysis. Chem. Mater. 35. https://doi.org/10.1021/acs.chemmater.3c00215.

Du, Z., Li, B., Jiang, C., Sun, R., Chen, S., 2021. Sorption of U(VI) on Schiff-base functionalized metal–organic frameworks UiO-66-NH_2. J Radioanal Nucl Chem 327. https://doi.org/10.1007/s10967-020-07550-6.

El-Mehalmey, W.A., Ibrahim, A.H., Abugable, A.A., Hassan, M.H., Haikal, R.R., Karakalos, S.G., Zaki, O., Alkordi, M.H., 2018. Metal-organic framework@silica as a stationary phase sorbent for rapid and cost-effective removal of hexavalent chromium. J Mater Chem A Mater 6. https://doi.org/10.1039/c7ta08281a.

Fan, H., Zhang, Z., Chen, Y., Wang, Z., Wen, H., Tian, S., Chen, S., Zhao, H., He, Y., Wang, Y., 2023. Post-synthetic modification (PSM) of MOFs with an ionic polymer for efficient adsorptive removal of methylene blue from water. Dalton Trans. 52. https://doi.org/10.1039/d3dt00852e.

Feil, F., Cauda, V., Bein, T., Bräuchle, C., 2012. Direct visualization of dye and oligonucleotide diffusion in silica filaments with collinear mesopores. Nano Lett 12. https://doi.org/10.1021/nl2039474.

Gebre Meskel, A., Kwikima, M.M., Meshesha, B.T., Habtu, N.G., Naik, S.V.C.S., Vellanki, B.P., 2024. Malachite green and methylene blue dye removal using modified bagasse fly ash: Adsorption optimization studies. Environmental Challenges 14. https://doi.org/10.1016/j.envc.2023.100829.

Gómez-Avilés, A., Solís, R.R., García-Frutos, E.M., Bedia, J., Belver, C., 2023. Novel isoreticular UiO-66-NH_2 frameworks by N-cycloalkyl functionalization of the 2-aminoterephtalate linker with enhanced solar photocatalytic degradation of acetaminophen. Chem. Eng. J. 461. https://doi.org/10.1016/j.cej.2023.141889.

Grimm, A., dos Reis, G.S., Dinh, V.M., Larsson, S.H., Mikkola, J.P., Lima, E.C., Xiong, S., 2024. Hardwood spent mushroom substrate–based activated biochar as a sustainable bioresource for removal of emerging pollutants from wastewater. Biomass Convers Biorefin 14. https://doi.org/10.1007/s13399-022-02618-7.

Güdücü, I., Alper, K., Evcil, T., Tekin, K., Ohtani, H., Karagöz, S., 2021. Effects of hydrothermal carbonization on products from fast pyrolysis of cellulose. J. Energy Inst. 99. https://doi.org/10.1016/j.joei.2021.10.004.

Han, S., Yang, J., Lin, X., 2021. Removal of methylene blue from aqueous solution by functionalized UiO-66 with basic moiety. Desalination Water Treat 213. https://doi.org/10.5004/dwt.2021.26725.

Hashem, T., Ibrahim, A.H., Wöll, C., Alkordi, M.H., 2019. Grafting Zirconium-Based Metal-Organic Framework UiO-66-NH_2 Nanoparticles on Cellulose Fibers for the Removal of Cr(VI) Ions and Methyl Orange from Water. ACS Appl Nano Mater 2. https://doi.org/10.1021/acsanm.9b01263.

Hegazy, S., Abdelwahab, Nour.A., Ramadan, Ahmed.M., Mohamed, Sahar.K., 2024. Magnetic Fe_3O_4-grafted cellulose/graphene oxide nanocomposite for methylene blue removal from aqueous solutions: Synthesis and characterization. Next Materials 3, 100064. https://doi.org/10.1016/j.nxmate.2023.100064.

Hegazy, S.H., Mohamed, S.K., 2021. Starch-graft-polyacrylamide copolymer /Fe_3O_4 /graphene oxide nanocomposite: synthesis, characterization, and application as a low-cost adsorbent for Ni (II) from aqueous solutions. J. Polym. Res. 28. https://doi.org/10.1007/s10965-020-02275-2.

Hegde, V., Uthappa, U.T., Suneetha, M., Altalhi, T., Soo Han, S., Kurkuri, M.D., 2023. Functional porous Ce-UiO-66 MOF@Keratin composites for the efficient adsorption of trypan blue dye from wastewater: A step towards practical implementations. Chemical Engineering Journal 461. https://doi.org/10.1016/j.cej.2023.142103.

Huang, L., Cao, H., Ma, J., Wang, X., 2022. Efficient removal of Pb(II) by UiO-66-NH_2: A combined experimental and spectroscopic studies. Environ Nanotechnol Monit Manag 18. https://doi.org/10.1016/j.enmm.2022.100741.

Huang, H., Chen, Z., Amesh, P., Kumar, S., Kumar, A., Ma, S., Li, S., Shi, W., Yang, X., Ren, P., 2024. Insights into the adsorption mechanism of the selenite ion in a cationic metal–organic framework. Chem. Eng. J. 497. https://doi.org/10.1016/j.cej.2024.154665.

Ighalo, J.O., Iwuozor, K.O., Igwegbe, C.A., Adeniyi, A.G., 2021. Verification of pore size effect on aqueous-phase adsorption kinetics: A case study of methylene blue. Colloids Surf A Physicochem Eng Asp 626. https://doi.org/10.1016/j.colsurfa.2021.127119.

Kang, D.A., Murphy, C., Jeong, H.K., 2024. Improving CO_2 adsorption capacity and CO_2/N_2 selectivity of UiO-66-NH_2 via defect engineering and IL-encapsulation. Microporous Mesoporous Mater. 369. https://doi.org/10.1016/j.micromeso.2024.113038.

Kebede Gurmessa, B., Taddesse, A.M., Teju, E., 2023. UiO-66 (Zr-MOF): Synthesis, Characterization, and Application for the Removal of Malathion and 2, 4-D from Aqueous Solution. Environmental Pollutants and Bioavailability 35. https://doi.org/10.1080/26395940.2023.2222910.

Kubo, M., Miyoshi, Y., Uchitomi, Y., Shimada, M., 2024. Insights into the Spray Synthesis of UiO-66 and UiO-66-NH_2 Metal-Organic Frameworks: Effect of Zirconium Precursors and Process Parameters. Crystals (basel) 14. https://doi.org/10.3390/cryst14020116.

Kumar Prajapati, A., Kumar Mondal, M., 2022. Green synthesis of Fe_3O_4-onion peel biochar nanocomposites for adsorption of Cr(VI), methylene blue and congo red dye from aqueous solutions. J Mol Liq 349. https://doi.org/10.1016/j.molliq.2021.118161.

Lei, Y., Xie, J., Quan, W., Chen, Q., Wang, A., 2024. Advances in adsorption of Pb(II) by MOFs-based nanocomposites in water. Prog. Nat. Sci.: Mater. Int. 34. https://doi.org/10.1016/j.pnsc.2024.02.005.

Liu, F., Li, W., Zhou, Y., 2021. Preparation and characterization of magnetic sodium alginate-modified zeolite for the efficient removal of methylene blue. Colloids Surf A Physicochem Eng Asp 629. https://doi.org/10.1016/j.colsurfa.2021.127403.

Liu, J., Wang, N., Zhang, H., Baeyens, J., 2019. Adsorption of Congo red dye on $Fe_xCo_{3-x}O_4$ nanoparticles. J Environ Manage 238. https://doi.org/10.1016/j.jenvman.2019.03.009.

Luu, C.L., Van Nguyen, T.T., Nguyen, T., Hoang, T.C., 2015. Synthesis, characterization and adsorption ability of UiO-66-NH_2. Adv. Nat. Sci. Nanosci. Nanotechnol. 6. https://doi.org/10.1088/2043-6262/6/2/025004.

N. Mahmud, L. Yasser, R.B.H. Mahmoud, A. Benamor, Adsorption of Congo Red Dye Using Activated Carbon-Fe3O4 Composite, in: Proceedings of the 2nd International Conference on Civil Infrastructure and Construction (CIC 2023), 2023. https://doi.org/10.29117/cic.2023.0163.

Meng, Y., Wang, Y., Li, G., Liu, G., Wang, L., 2024. Insight into the adsorption behavior and mechanism of trace impurities from H_2O_2 solution on functionalized zirconia by tuning the structure of amino groups. Front Chem Sci Eng 18. https://doi.org/10.1007/s11705-024-2415-3.

Mousavi, D.V., Ahmadipouya, S., Shokrgozar, A., Molavi, H., Rezakazemi, M., Ahmadijokani, F., Arjmand, M., 2021. Adsorption performance of UiO-66 towards organic dyes: Effect of activation conditions. J Mol Liq 321. https://doi.org/10.1016/j.molliq.2020.114487.

Ngobeni, W.A., Mulaba-Bafubiandi, A.F., 2023. Investigating the thermodynamics and adsorption mechanisms of alkaline gelatinised novel depressants on pyrite surface. J Mol Liq 384. https://doi.org/10.1016/j.molliq.2023.122173.

Niu, T., Zhou, J., Zhang, C., Li, S., 2018. Fast removal of methylene blue from aqueous solution using coal-based activated carbon. RSC Adv 8. https://doi.org/10.1039/c8ra04396e.

Olchowski, R., Giannakoudakis, D.A., Anastopoulos, I., Barczak, M., Zięba, E., Dobrowolski, R., Dobrzyńska, J., 2021. Arsenazo III removal from diagnostic laboratories wastewater by effective adsorption onto thermochemically modified ordered mesoporous carbon. Environ Nanotechnol Monit Manag 16. https://doi.org/10.1016/j.enmm.2021.100607.

Pandey, A., Qamar, S.F., Das, S., Basu, S., Kesarwani, H., Saxena, A., Sharma, S., Sarkar, J., 2024. Advanced multi-wall carbon nanotube-optimized surfactant-polymer flooding for enhanced oil recovery. Fuel 355. https://doi.org/10.1016/j.fuel.2023.129463.

Peng, R., Zhang, S., Yao, Y., Wang, J., Zhu, X., Jiang, R., Zhang, J., Zhang, W., Wang, C., 2023. MOFs meet electrospinning: New opportunities for water treatment. Chem. Eng. J. 453. https://doi.org/10.1016/j.cej.2022.139669.

Rabiee, N., 2023. Sustainable metal-organic frameworks (MOFs) for drug delivery systems. Mater Today Commun 35. https://doi.org/10.1016/j.mtcomm.2023.106244.

Salmani Nuri, O., Irannajad, M., Mehdilo, A., 2019. Reagent adsorption on modified mineral surfaces: isotherm, kinetic and thermodynamic aspects. J Mol Liq 291. https://doi.org/10.1016/j.molliq.2019.111311.

Shahzad, U., Marwani, H.M., Saeed, M., Asiri, A.M., Althomali, R.H., Rahman, M.M., 2023. Exploration of porous metal-organic frameworks (MOFs) for an efficient energy storage applications. J Energy Storage 74. https://doi.org/10.1016/j.est.2023.109518.

Solís, R.R., Peñas-Garzón, M., Belver, C., Rodriguez, J.J., Bedia, J., 2022. Highly stable UiO-66-NH_2 by the microwave-assisted synthesis for solar photocatalytic water treatment. J Environ Chem Eng 10. https://doi.org/10.1016/j.jece.2021.107122.

Taddei, M., van Bokhoven, J.A., Ranocchiari, M., 2020. Influence of Water in the Synthesis of the Zirconium-Based Metal–Organic Framework UiO-66: Isolation and Reactivity of $[ZrCl(OH)_2(DMF)_2]Cl$. Inorg. Chem. 59, 7860–7868. https://doi.org/10.1021/acs.inorgchem.0c00991.

Thomas, A., 1996. Unger. William Andrew Publishing, Pesticide Synthesis Handbook.

Timofeev, K.L., Kulinich, S.A., Kharlamova, T.S., 2023. NH_2-Modified UiO-66: Structural Characteristics and Functional Properties. Molecules 28. https://doi.org/10.3390/molecules28093916.

Wang, T., Han, L., Li, X., Chen, T., Wang, S., 2022. Functionalized UiO-66-NH_2 by trimellitic acid for highly selective adsorption of basic blue 3 from aqueous solutions. Front Chem 10. https://doi.org/10.3389/fchem.2022.962383.

Wen, L., Chen, X., Chen, C., Yang, R., Gong, M., Zhang, Y., Fu, Q., 2020. Ice-templated porous polymer/UiO-66 monolith for Congo Red adsorptive removal. Arab. J. Chem. 13. https://doi.org/10.1016/j.arabjc.2020.04.007.

Wu, X., Gao, Y., Bi, J., 2024. Understanding the structure-dependent adsorption behavior of four zirconium-based porphyrinic MOFs for the removal of pharmaceuticals. Microporous Mesoporous Mater. 363. https://doi.org/10.1016/j.micromeso.2023.112827.

Yazdi, F., Sepehrian, M., Anbia, M., 2024. Selective removal of trace Pb(II) from water using tin dioxide nanoparticle-modified porous materials: A comprehensive study on batch, and fixed-bed column adsorption. J. Water Process Eng. 64. https://doi.org/10.1016/j.jwpe.2024.105532.

Yu, K., Huan, W.W., Teng, H.J., Guo, J.Z., Li, B., 2024. Effect of oxygen-containing functional group contents on sorption of lead ions by acrylate-functionalized hydrochar. Environ. Pollut. 349. https://doi.org/10.1016/j.envpol.2024.123921.

Yu, S., Pang, H., Huang, S., Tang, H., Wang, S., Qiu, M., Chen, Z., Yang, H., Song, G., Fu, D., Hu, B., Wang, X., 2021. Recent advances in metal-organic framework membranes for water treatment: A review. Sci. Total Environ. 800. https://doi.org/10.1016/j.scitotenv.2021.149662.

Yusop, M.F.M., Yahaya, N.K.E.M., Karim, J., Yusoff, M.A.M., Abdullah, A.Z., Ahmad, M. A., 2023. Synthesis of Microwave-Assisted Mango Peel Based Activated Carbon for Methylene Blue Dye Removal. Green Energy and Technology. https://doi.org/10.1007/978-981-99-1695-5_21.

Zhang, H., Shi, X., Li, J., Kumar, P., Liu, B., 2019. Selective dye adsorption by zeolitic imidazolate framework-8 loaded UiO-66-NH_2. Nanomaterials 9. https://doi.org/10.3390/nano9091283.

Zhou, T., Yang, D., Wang, Y., Cheng, J., Chen, Q., Liu, B., Liu, Z., 2023. Low-pressure-RF plasma modification of UiO-66 and its application in methylene blue adsorption. Plasma Sci. Technol 25. https://doi.org/10.1088/2058-6272/acc3d2.